Supershear source model of the 2025 M7.8 Myanmar earthquake and paleoseismology of the Sagaing Fault: regions of significant overlap with past earthquakes

D. Melgar[1,*], R. Weldon[1], Wang Y.[2], M.G. Bato[3], L.T. Aung[4], Shi X.[5], W. Wiwegwin[6], S.N. Khaing[7], S. Min[8], M. Thant[9], C.M. Speed[3], R. Zinke[3], E.J. Fielding[3], A.J. Meltzner[4,10], T. Dawson[11]

[1] *Department of Earth Sciences, University of Oregon, Eugene, OR, USA*
[2] *Department of Geosciences, National Taiwan University, Taipei, Taiwan*
[3] *Jet Propulsion Laboratory, California Institute of Technology, Pasadena, CA, USA*
[4] *Earth Observatory of Singapore, Nanyang Technological University, Singapore*
[5] *Zhejiang University, Hangzhou, China*
[6] *Department of Mineral Resources, Bangkok, Thailand*
[7] *Department of Geology, Hinthada University, Myanmar*
[8] *Dept of Geology, Banmaw University, Myanmar*
[9] *Myanmar Institute of Earth and Planetary Sciences, and University of Yangon, Myanmar*
[10] *Asian School of the Environment, Nanyang Technological University, Singapore*
[11] *California Geological Survey, San Mateo, CA, USA*

[*] Corresponding author: dmelgarm@uoregon.edu

Author contributions

- Conceptualization: D.M., R.W.,Y.W., M.G.B., L.T.A.,X.S.,W.W.
- Formal analysis: All authors
- Software: D.M., M.G.B., C.M.S., R.Z., E.J.F.
- Visualization: D.M., R.W., W.Y., L.T.
- Funding Acquisition: D.M., R.W., M.G.B., Y.W.,X.S.
- Writing – original draft: D.M., R.W.
- Writing – review & editing: All authors

Abstract

The 2025 Mw 7.8 earthquake on the central Sagaing Fault is one of the most destructive seismic events in Myanmar's recorded history, producing near-fault shaking exceeding Modified Mercalli Intensity X and impacting tens of millions of people across Southeast Asia. We present a detailed kinematic rupture model of the event based on joint inversion of regional strong motion waveforms and Sentinel-1 SAR pixel offsets. The rupture extended over ~450 km with an average slip of 3–5 m, predominantly within the upper 10 km of the crust. Inversions favor a maximum rupture speed of ~4.8 km/s, consistent with supershear propagation inferred from near-field waveform observations. We also report on paleoseismic evidence from a key site at the epicenter of the 2025 earthquake near Mandalay, which reveals at least five surface-rupturing earthquakes over the past millennium, with similar average displacement. Our results indicate a pattern of overlapping large ruptures along the central fault, with implications for segmentation, recurrence, and seismic hazard. Given the exceptional exposure and high strain rates, our findings underscore the need for urgent attention to earthquake preparedness and infrastructure resilience in central Myanmar.

Second language abstract: Burmese

စစ်ကိုင်းပြတ်ရွေ့ အလယ်ပိုင်းတွင် ဗဟိုပြုလှုပ်ခတ်ခဲ့သော ပြင်းအား ၇.၈ အဆင့်ရှိ ၂၀၂၅ ငလျင်သည် မြန်မာ့ငလျင်သမိုင်းမှတ်တမ်းတွင် အပျက်အစီးအကြီးမားဆုံးငလျင်များထဲမှ တစ်ခုဖြစ်ပြီး၊ ပြတ်ရွေ့အနီးတလျှောက်တွင် ငလျင်ဒဏ်ခံစားရမှု မာကယ်လီ စကေး ၁၀ အထက်ရှိကာ၊ အရှေ့တောင်အာရှတစ်လွှားရှိ လူဦးရေ သန်းပေါင်းများစွာအပေါ် ကို သက်ရောက်မှုရှိခဲ့သည်။ ဆန်တီနယ်-၁ ဂြိုလ်တုပုံရိပ်များ၏ (Sentinel-1 InSAR pixel offsets) ပုံရိပ်အစက်အပြောက်အရွေ့များနှင့် ဒေသတွင်းငလျင်လှိုင်းမှတ်တမ်းများကို အခြေခံပေါင်းစပ်အသုံးပြု၍ ယခုငလျင်၏ မြေပြင်ရွေ့ပြတ်မှုအသေးစိတ်ပုံစံကို သုံးသပ်တင်ပြထားပါသည်။ မြေပြင်ရွေ့ပြတ်မှုသည် ကမ္ဘာ့အပေါ်ယံလွှာ၏ ၁၀ ကီလိုမီတာအတွင်းတွင် ပျမ်းမျှအရွေ့ ၃ - ၅ မီတာခန့်ရှိပြီး၊ အရှည်အားဖြင့် ၄၅၀ ကီလိုမီတာဝန်းကျင်ခန့်အထိ ရွေ့ပြတ်မှု ဖြစ်ခဲ့သည်။ ငလျင်လှုပ်ခတ်သော ပြတ်ရွေ့အနီး တိုင်းတာမှတ်တမ်းတင်ထားသော ငလျင်လှိုင်းများကို လေ့လာဆန်းစစ်မှုများအရ အမြင့်ဆုံးရွေ့ပြတ်နှုန်းသည် ၁ စက္ကန့်တွင် ၄.၈ ကီလိုမီတာ နှုန်းဖြင့် ရွေ့ပြတ်ခဲ့သောကြောင့်၊ မြန်နှုန်းမြင့်သော ဖျက်အားပြင်းငလျင် အမျိုးအစားဖြစ်ကြောင်း ကောက်ချက်ချနိုင်သည်။ မန္တလေးမြို့အနီး ၂၀၂၅ ခုနှစ်ငလျင်ဗဟိုချက်ဝန်းကျင်ရှိ အဓိကနေရာမှ အတိတ်ငလျင်ဆိုင်ရာ အထောက်အထား မှတ်တမ်းများအရ လွန်ခဲ့သော ထောင်စုနှစ်အတွင်း မျက်နှာပြင်ရွေ့ပြတ်မှုရှိခဲ့သော ငလျင်များ အနည်းဆုံး ငါးကြိမ်ခန့်လှုပ်ခတ်ခဲ့ပြီး တူညီသော ပျမ်းမျှရွေ့ပြတ်မှုပမာဏရှိခဲ့သည်ကိုလည်း တွေ့ရသည်။ ကျွန်ုပ်တို့၏လေ့လာတွေ့ရှိချက် ရလဒ်များသည် ပြတ်ရွေ့အဆစ်အပိုင်းများ ပိုင်းခြားသတ်မှတ်ခြင်း၊ ငလျင်များ ပြန်လည်လှုပ်ခတ်မှုအချိန်ကာလ နှင့် ပြင်းအားပမာဏ၊ ငလျင်အန္တရာယ် စသည့်အကျိုးသက်ရောက်မှုများနှင့်အတူ စစ်ကိုင်းပြတ်ရွေ့၏ အလယ်ပိုင်းတလျှောက်တွင် ပမာဏကြီးမားရှည်လျားသော ငလျင်ရွေ့ပြတ်မှု၊ ပြတ်ရွေ့အဆစ်အပိုင်းများ တစ်ခုနှင့်တစ်ခုထပ်နေသော ပုံစံကို လေ့လာတွေ့ရှိရသည်။ လူဦးရေ၊ အဆောက်အဦ၊ အခြေခံအဆောက်အအုံများ အလွန်မြင့်မားမှု၊ စစ်ကိုင်းပြတ်ရွေ့တစ်လျှောက် ပုံပျက်ယွင်းမှုနှုန်းမြင့်မားခြင်းတို့ကြောင့် မြန်မာနိုင်ငံတွင် ငလျင်ဘေးအန္တရာယ် လျော့ကျရေးဆိုင်ရာ ကြိုတင်လေ့ကျင့် ပြင်ဆင်မှုနှင့် အခြေခံအဆောက်အအုံများ၏ ခံနိုင်ရည်ရှိရေးတို့အား အရေးပေါ်အဆင့် အာရုံစိုက်ဆောင်ရွက်ရန် လိုအပ်ကြောင်း ကျွန်ုပ်တို့၏ လေ့လာတွေ့ရှိချက်များက ညွှန်းဆိုနေသည်။

Second language abstract: Thai

เมื่อวันที่ 28 มีนาคม 2568 เกิดแผ่นดินไหวขนาด 7.8 ตามมาตราโมเมนต์ (Mw) มีสาเหตุเกิดจากการเลื่อนตัวของรอยเลื่อนสะกาย ถือเป็นหนึ่งในเหตุการณ์แผ่นดินไหวที่สร้างความเสียหายมากที่สุดในประวัติศาสตร์ของประเทศเมียนมา โดยมีระดับความรุนแรงของแผ่นดินไหวมากกว่าระดับ X ตามมาตราเมอร์คัลลี่ดัดแปลง (Modified Mercalli Intensity) ในบริเวณใกล้กับตำแหน่งของรอยเลื่อนสะกาย แรงสั่นสะเทือนของแผ่นดินไหวสามารถรับรู้ได้ในหลายประเทศและส่งผลกระทบต่อประชากรนับสิบล้านคนในภูมิภาคเอเชียตะวันออกเฉียงใต้ ผลการศึกษานี้ได้เสนอแบบจำลองการเกิดแนวรอยแตกของพื้นผิวดินด้วยการวิเคราะห์จลนศาสตร์แบบผกผัน (kinematic rupture model) โดยอาศัยข้อมูลคลื่นสั่นสะเทือนของพื้นดินที่ถูกบันทึกจากสถานีตรวจวัดแผ่นดินไหวในภูมิภาค และข้อมูลการเปลี่ยนรูปของพื้นผิวดินจากดาวเทียม Sentinel-1 ผลการวิเคราะห์พบว่าแนวรอยแตกของพื้นผิวดินจากเหตุการณ์แผ่นดินไหวมีระยะทางประมาณ 450 กิโลเมตร มีระยะการเลื่อนตัวเฉลี่ยอยู่ที่ 3–5 เมตร และส่วนใหญ่จะเกิดขึ้นในชั้นเปลือกโลกส่วนบนที่ความลึกไม่เกิน 10 กิโลเมตร การเลื่อนตัวของแนวรอยแตกมีความเร็วสูงสุดประมาณ 4.8 กิโลเมตรต่อวินาที ซึ่งสอดคล้องกับรูปแบบการเกิดแผ่นดินไหวที่มีความเร็วของแนวรอยแตกเหนือความเร็วเฉือน (supershear) คณะผู้ศึกษายังพบหลักฐานการเกิดแผ่นดินไหวโบราณอย่างน้อย 5 เหตุการณ์ ในช่วง 1,000 ปีที่ผ่านมา ในร่องสำรวจใกล้เมืองมัณฑะเลย์ซึ่งเป็นตำแหน่งของศูนย์กลางของแผ่นดินไหวครั้งนี้ โดยเหตุการณ์แผ่นดินไหวโบราณดังกล่าวทำให้เกิดระยะการเลื่อนตัวของรอยเลื่อนในแต่ละครั้งมีระยะทางที่ใกล้เคียงกัน ผลการศึกษาในครั้งนี้ยังบ่งชี้ให้เห็นถึงรูปแบบของการเกิดแผ่นดินไหวขนาดใหญ่ในพื้นตอนกลางของแนวรอยเลื่อนสะกาย และสามารถนำไปใช้ประโยชน์ในการกำหนดตำแหน่งของรอยเลื่อนย่อย การเกิดแผ่นดินไหวซ้ำ และการประเมินภัยพิบัติแผ่นดินไหว บริเวณตอนกลางของประเทศเมียนมา เป็นพื้นที่เสี่ยงภัยจากแผ่นดินไหวสูง เนื่องจากมีสิ่งก่อสร้าง อาคาร และผู้คนอาศัยอยู่เป็นจำนวนมาก และมีอัตราการการเปลี่ยนรูปของหินหรือชั้นเปลือกโลกที่สูง ดังนั้น จึงมีความจำเป็นเร่งด่วนที่จะต้องให้ความสำคัญต่อการเตรียมความพร้อมรับมือแผ่นดินไหว และการเสริมสร้างความมั่นคงแข็งแรงของโครงสร้างพื้นฐานในบริเวณดังกล่าว

Second language abstract: Traditional Chinese

2025年發生於實皆斷層中段的曼德勒地震(Mw 7.8)是緬甸史上最嚴重的災害性地震之一，於斷層周邊地區造成超過修訂麥卡利震度分級(MMI)10級以上的強烈強地動，並對東南亞地區上千萬人產生影響。本研究透過強震地震波形與哨兵一號衛星合成孔徑雷達像素偏移資料進行聯合反演，建立本次地震的斷層破裂運動模型。研究成果指出本次地震的同震位

移達3-5公尺，破裂長度超過450公里，主要破裂集中在地殼淺部10公里內的斷層面上。模型中最大地震破裂傳播速度可達~4.8公里/秒，與近斷層的地震波觀測資料所指出的超剪切地震傳播型態相符。本研究位於2025年地震震央附近的古地震槽溝亦發現該段斷層在過去約1000年期間中發生了至少5次的地表破裂事件，且每次事件皆具有相似的錯移量。我們的古地震研究成果暗示實皆斷層中段具有大型的重疊破裂特性，對該斷層的孕震區段、破裂週期與地震災害分析都有一定程度的影響。有鑑於緬甸中部的高地震風險暴露度與高應變率，本研究認為該地區的基礎建設韌性與地震災害防備皆急需特別的關注。

Second language abstract: Simplified Chinese

2025年发生于实皆断层中段的曼德勒地震(Mw 7.8)是缅甸历史上最严重的灾害性地震之一。该地震造成断层周边地区的强烈地动——修订麦卡利震度分级(MMI)达10级以上，并对东南亚地区上千万人产生重要影响。本研究透过强震地震波形与哨兵一号卫星合成孔径雷达像素偏移资料进行联合反演，建立本次地震的断层破裂运动模型。研究成果表明，本次地震的同震位移达3-5米，破裂长度超过450公里，主要破裂集中在地壳浅部10公里内的断层面上。模型中最大地震破裂传播速度可达~4.8公里/秒，与近断层的地震波观测资料所指出的超剪切地震传播型态相符。而位于2025年地震震中附近的古地震探槽也发现：该段断层在过去约1000年期间中发生了至少5次的地表破裂事件，且每次事件均具有相似的同震位错量。我们的古地震研究成果揭示，实皆断层中段具有大型的重叠破裂特性，对该断层的孕震区段、破裂周期和地震灾害分析都有一定程度的影响。鉴于缅甸中部的高地震风险程度与高应变率，本研究认为该地区的基础建设韧性与地震灾害防备亟需特别关注。

Non-technical summary

On March 28, 2025, a powerful magnitude 7.8 earthquake struck central Myanmar along the Sagaing Fault, causing severe shaking near the fault and damage as far away as Bangkok, Thailand. Nearly 18 million people experienced strong shaking, and while the official death toll is around 4,000, the true number is likely much higher due to limited access and reporting in conflict zones. Using ground sensors and satellite data, scientists found the rupture extended about 450 kilometers with 3-5 meters of movement along the fault. The fault broke at unusually high speed—a phenomenon called "supershear"—which can generate especially strong shaking. Trenches dug across the fault in 2016 & 2018 revealed that this same section has broken in multiple past earthquakes, including in 1839, and the 1946/1956 sequence. These findings show that large earthquakes repeatedly strike this part of the fault. Because the region is heavily populated and rapidly developing, the Sagaing Fault remains a major hazard. Improving construction standards, emergency preparedness, and continued research are essential to reduce future risk.

1. Overview of the event and the Sagaing fault

The 2025 Mw 7.8 Myanmar earthquake represents a landmark event in the seismic history of the country and the broader Southeast Asian region (Thein et al., 2009; Hurukawa et al., 2011; Wang et al., 2014). The U.S. Geological Survey's ShakeMap (USGS, 2017, Figure 1A) shows that near-fault areas experienced extreme shaking intensities, with Modified Mercalli Intensity (MMI) levels exceeding X, causing widespread destruction. The event's regional importance is underscored as well by the high population densities surrounding the fault: according to the PAGER system (Prompt Assessment of Global Earthquakes for Response; Earle et al., 2009; Wald et al., 2010), also from the USGS, which estimates human and economic impacts, approximately 17.8 million people were exposed to shaking of MMI VII or greater, and 6.2 million people to MMI IX or greater (USGS, 2025). The shaking was so intense that damage and strong ground motions were reported as far away as Bangkok, Thailand. At the time of this writing, official fatality counts are approximately 4,000. However, given the extraordinary exposure to severe shaking, known structural vulnerabilities in Myanmar and neighboring regions, it is likely that the true number of fatalities is significantly larger. This is especially true because of the complicating factor of an ongoing civil conflict that impairs accurate reporting and emergency response—it is well-established that impacts from natural disaster in conflict areas are systematically under-reported (e.g. NRC, 2007).

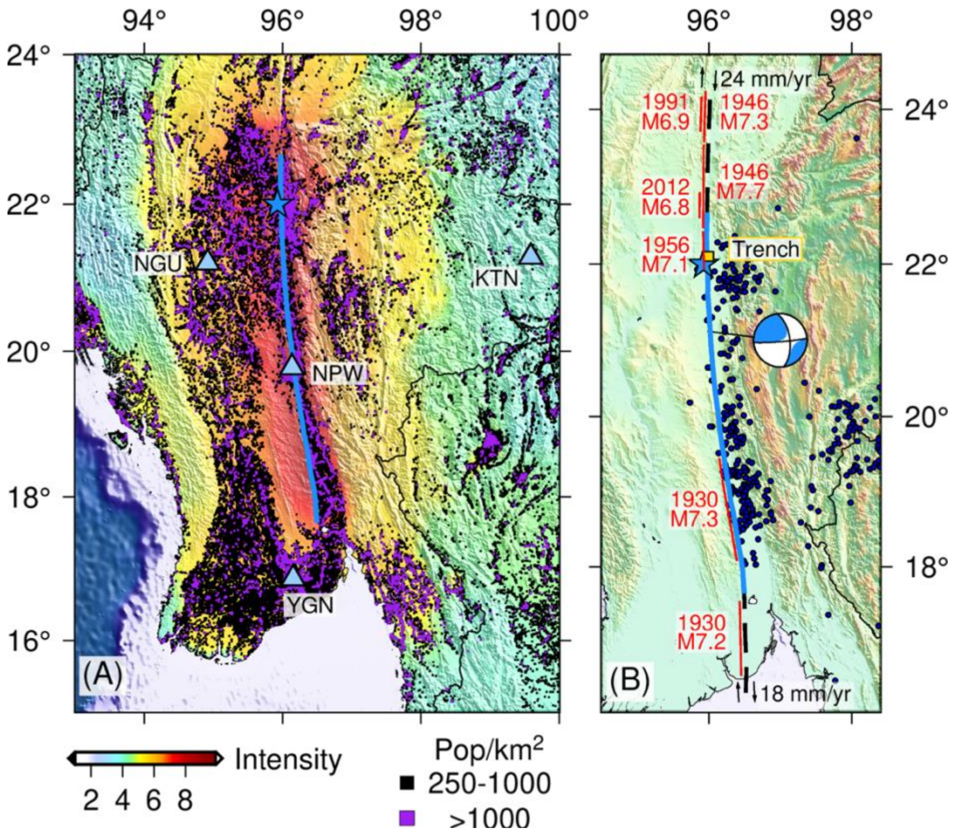

Figure 1. *(A) Overview of shaking intensity from USGS ShakeMap (USGS, 2017) and impacts to the population from the M7.8 earthquake. Population density data is from LandScan (Lebakula et al., 2024) (B) Tectonic overview of the Sagaing Fault, past ruptures estimated lengths are from (Wang et al., (2017), moment tensor for the mainshock is from the global CMT project (Ekstrom et al., 2012) and 2 weeks of aftershocks are from the Thailand National Seismic Network (Pornsopin et al., 2023). Shown as well is the slip-rate estimate for the Sagaing Fault from Tin et al. (2022) and the location of a trench site used to establish the paleoseismic history of the fault in this work.*

Myanmar occupies a geologically complex and tectonically active region (Figure 1B) at the intersection of the Indian, Sunda, and Eurasian plates (e.g., Socquet et al., 2006; Gahalaut and Gahalaut, 2007). The oblique convergence between the Indian and Sunda plates is accommodated by a combination of subduction, strike-slip faulting and block extrusion processes (Wang et al., 2014; Shi et al., 2018; Mallick et al., 2019). To the west, the Rakhine-Bangladesh megathrust marks the zone of north-eastward subduction of the Indian plate beneath the Burma plate, forming the Indo-Burman ranges. To the east, the prominent right-lateral Sagaing Fault (on which the 2025 event occurred) serves as the principal boundary between the Burma plate and the Sundaland block (Socquet et al., 2006; Wang et al., 2014; Mallick et al., 2019; Tin et al., 2022; Lindsey et al., 2023). Between these two major structures lies the Central Myanmar Belt (CMB), an elongate lowland region bounded by active deformation on both sides. Geodetic measurements show that the Indian plate is moving northeastward relative to the Sunda plate at a rate of approximately 35 mm/yr near 10°N, with the Sagaing Fault accommodating roughly 18–24 mm/yr of right-lateral strike-slip motion (Steckler et al., 2016; Tin et al., 2022; Lindsey et al., 2023). The remaining convergence is partitioned across the Rakhine-Bangledsh megaturst, the Indo-Burman fold and thrust belt and the Central Myanmar Belt west of the Sagaing Fault. Historical and instrumental records indicate that the region can produce large and damaging earthquakes, posing significant seismic hazards, especially for rapidly growing urban centers like Yangon, Nay Pyi Taw, and Mandalay (e.g. Le Dain et al., 1984; Hurukawa and Phyu Maung Maung, 2011; Xiong et al., 2017).

The Sagaing Fault is a major north-south striking right-lateral strike-slip fault extending over 1,200 km from the Andaman Sea in the south to the eastern Himalayan syntaxis in the north (e.g., Maung, 1987; Curray, 2005). It accommodates the primary component of dextral shear between the Burma and Sunda plates. Formed most likely in the late Oligocene (Morley and Arboit, 2019), the fault has recorded a cumulative displacement of 330–450 km (e.g., Maung, 1987; Wang et al., 2011; Soe Thura Tun and Watkinson, 2017; Xiong et al., 2017). Modern GNSS observations reveal that the fault's slip rate varies along strike, with ~23–24 mm/yr measured along central segments and somewhat slower rates (~16 mm/yr) inferred for southern segments with workers suggesting potentially variable dips from sub-vertical to vertical along-strike (Mon et al., 2020; Tin et al., 2022; Yang et al., 2024). The fault is segmented into several distinct sections, including the Sagaing, Meiktila, and Bago segments in the south (e.g. Wang et al., 2014; Soe Thura Tun and Watkinson, 2017; Panda et al., 2018; Tin et al., 2022). Each segment exhibits varying degrees of locking and strain accumulation at depths of 10–16 km (Vigny et al., 2003; Socquet et al., 2006; Maurin et la., 2010; Tin et al., 2022). Stress transfer modeling over the past century, and the instrumental seismic catalog has identified seismic gaps along the central and southern Sagaing Fault, indicating regions of heightened seismic hazard. Notable historical earthquakes, such as the 1930 Bago, 1946 Sagaing, and 2012 Thabeikkyin earthquakes, underscore the fault's potential to produce large-magnitude events (Hurukawa et al., 2011; Wang et al., 2014).

In this fast report we highlight how the 2025 rupture fits within this broader tectonic history for the region by producing a detailed kinematic slip model based on joint inversion of regional strong motion data and remote sensing observations. We will discuss findings from trenches near the epicenter of the 2025 rupture which has evidence of the 1839 M7.7 and the 1946/56 M7.7/ 7.1 sequence and re-ruptured once more during the 2025 event.

2. Available Data and Methods

2.1 Regional Seismic Data

Three-component strong motion recordings from four regional stations (Figure 2), were processed to obtain ground displacement time series (see Data Availability). Raw acceleration data were first corrected for instrument gain using known calibration factors. Each component was then baselinecorrected and de-trended to remove any DC offset. To reduce long-period drift and high-frequency noise, we applied a zero-phase, 4-pole Butterworth bandpass filter with corner frequencies at 0.05 Hz and 0.4 Hz. The filtered acceleration time series were then numerically integrated twice—first to velocity, then to displacement—using trapezoidal integration. This process yielded waveforms which were then decimated from their native sample rates of 100 and 200 Hz down to 5 Hz, suitable for kinematic slip inversion. The farthest station, KTN, is ~370 km from the surface trace of the Sagaing Fault while the closest site, NPW, in the capital city of Nay Pyi Taw, is only 2.5 km from the surface trace (Figure 1A).

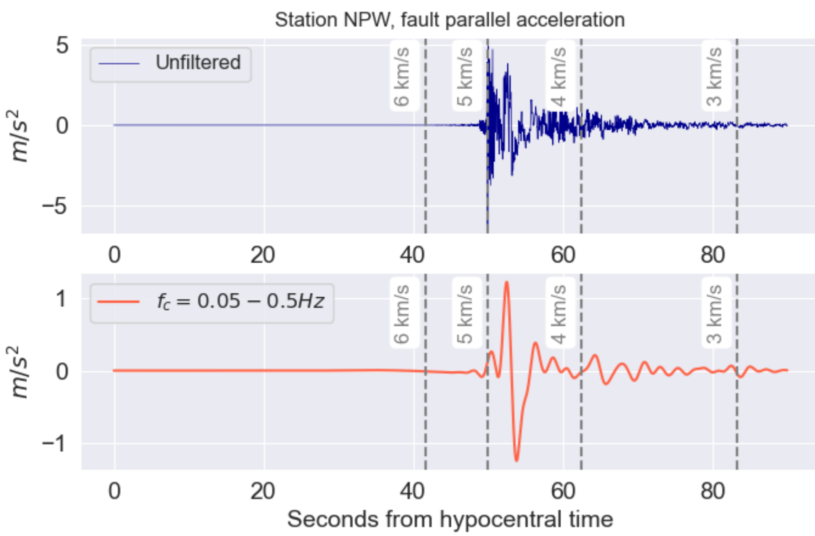

Figure 2. *Strong motion data from station NPW (location in Figure 1A). Plotted is the fault parallel acceleration without filtering and with a band pass filter applied. The main acceleration pulse is interpreted as the rupture transiting by the Sagaing fault on the segment closest to NPW. Dashed lines represent rupture velocities needed for the rupture pulse to reach NPW at specific times.*

NPW is particularly important because of its proximity to the fault, it is only 2.7 km from the surface rupture (Figure 1A,2); however, the network operator reported that approximately 3 days before the mainshock the station's GNSS antenna stopped working and the station lost absolute time (Lai et al., 2025). This means that without some form of calibration the data cannot be used for slip inversion. To correct for this, we use eight Mw>4.5 events that occurred in the vicinity of the mainshock hypocenter (Figure 1B) in the 5 years prior and for which absolute timing at the site is available. We picked the P-wave arrivals at NPW for each of these eight events, we estimated the theoretical P-wave arrival times by ray tracing from the catalog hypocenter to the location of NPW through a layered Earth model. We then obtain a "station delay" by taking the difference between the observed P-wave arrival time, t_{obs}, and the expected or modeled P-wave arrival time, t_{mod}. We noted that the delays are correlated to the station-event distance, so we also regressed for the best fit straight line of the station delays as a function of hypocentral distance. This linear model then allowed us to solve for the estimated theoretical arrival of the P-wave from the 2025 mainshock (red triangle in Figure 3) given its known hypocentral distance of 240 km. We compared this expected arrival to the observed arrival (yellow square in Figure 3). In this analysis we used three different velocity models, two global ones, PREM, and IASP91 (Dziewonski & Anderson, 1981; Kennet & Engdahl, 1991) and a regional lithospheric model (Pasyanos et al., 2014). We found that, while there are slight variations between velocity models, for all three the difference between the observed and expected P-wave arrival time for the 2025 mainshock is <1 s. From this we concluded that station NPW can be reliably used for slip inversion without further correction. This finding is consistent with Lai et al. (2025) who performed a similar analysis on other regional events and correlation of seismic noise and concluded likewise, that no station's clock had drifted more than 1s from the time the GNSS clock malfunctioned to the time of the mainshock.

2.2 Space geodetic data

We employed two sources of space geodetic data to estimate the coseismic displacements. First, we used near-infrared (band 8) optical imagery from the European Space Agency (ESA) Copernicus

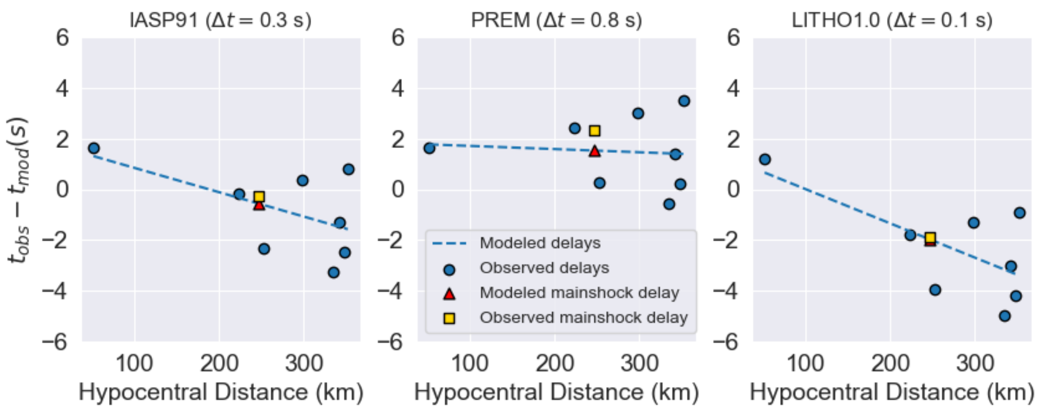

Figure 3. *Timing calibration for station NPW. Shown are the station delays for 8 Mw>4.5 regional events before the 2025 mainshock. These are the differences between expected P-wave arrival times from ray-tracing through a variety of velocity models and observed arrival times. The dashed line is the best fitting linear model as a function of hypocenter distance for these station delays. The yellow square is the observed delay for the mainshock and the red triangle the expected delay based on the best fitting model. The difference between them is shown in parentheses above each plot and is <1s for all three velocity models indicating that timing at NPW is reliable.*

Sentinel–2 Level 1C satellite imagery products (Drusch et al., 2012). We obtained north-south and east-west displacements by pixel offset tracking using two or more orthorectified and co-registered images acquired at different times (e.g., between 28 February and 6 April, 2025). To identify the shift in surface features between the images, we used the autonomous Repeat Image Feature Tracking (autoRIFT) software (Gardner et al., 2018; Lei et al., 2021), that measures offsets in the image row (north-south) and column (east-west) directions. These offsets, initially in pixel units, are then converted to ground displacements by multiplying them using the known pixel size (i.e., 10 meters for Sentinel-2 band 8). The result is a two-dimensional horizontal displacement field representing surface motion in the east-west and north-south directions. This technique is especially useful for mapping large, coherent motions such as glacier flow, landslides, or volcanic deformation. Though it is less precise than radar-based displacement-retrieval methods like InSAR (e.g. Strozzi et al., 2002; Casu et al., 2011), pixel tracking is more sensitive to north-south displacement and does not decorrelate in high-strain regions near the fault rupture (e.g., Avouac and Leprince, 2015). While we did not use these data in the inversion, they were used early on to determine the surface trace of the rupture and build the inversion geometry shown in Figure 1A,B.

Next, we utilized two pairs (Figure 4) of synthetic aperture radar (SAR) images from the European Space Agency's (ESA) Copernicus Sentinel-1A/B satellites—one pair for each track (ascending Track 143 and descending Track 106)—that captured the earthquake event. We measured the pixel offsets in both the range (across-track) and azimuth (along-track) directions using the Ampcor module within the ISCE2 software package [Rosen et al., 2012]. The pre- and post-earthquake Sentinel-1 Level-1 Single Look Complex (SLC) images were first co-registered using available restituted orbit files. We

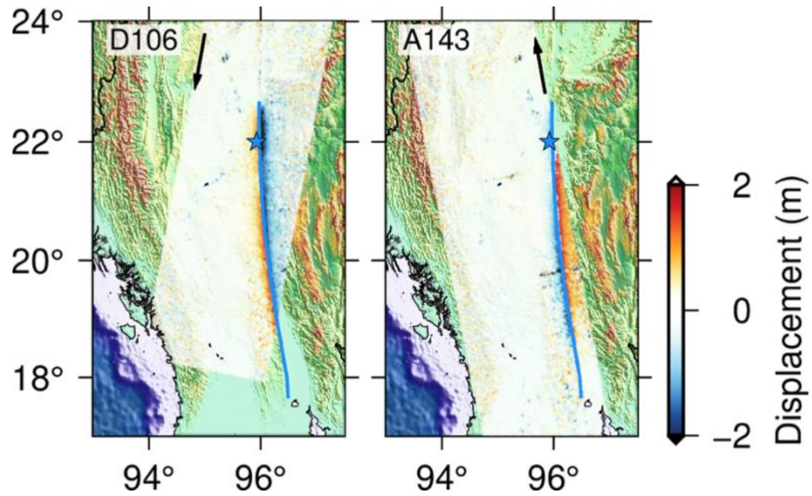

Figure 4. *Azimuth pixel offsets from InSAR ascending track 143 and descending track 106. Shown as well are east-west and north-south pixel offsets from optical Sentinel 2 observations. The blue line is the assumed fault trace and the star is the event hypocenter. The arrow in each scene indicates the satellite flight path, the offset displacement is thus the dot product of the horizontal coseismic deformation with this unit vector.*

performed cross-correlation between image patches in the reference and secondary scenes to determine sub-pixel shifts in both the range and azimuth directions. The measured offsets, initially in image coordinates, were converted to ground displacements using the sensor's known viewing geometry and pixel spacing. Range offsets correspond to displacements in the radar line-of-sight (LOS) direction, which has a strong east-west component for Sentinel-1's near-polar orbits and can include contributions from vertical land motion, while azimuth offsets capture motion along the satellite's trajectory and are primarily dominated by north-south deformation. Given the dextral north-south style of faulting, we prioritized the azimuth offsets. The resulting horizontal displacement fields are particularly robust for measuring large, decorrelating motions—such as coseismic rupture, glacier flow, volcanic deformation, and landslides—that may not be reliably captured with conventional interferometric phase techniques (e.g., Pathier et al., 2006; Casu et al., 2011; Bato et al., 2021; Lei et al., 2021).

As a final pre-inversion step, because the resulting scenes can be noisy, we apply a median filter with a window length of 1 km to remove short wavelength noise. These estimates of land motion are then obtained with a spacing of 3 arcsec (~90 m), which is far too dense for inversion—we decimate the data using uniform sampling and keep data within ~80 km of the surface trace; for each scene this is about 3000 pixels per acquisition.

2.3 Kinematic Inversion

The first step in the kinematic inversion is defining the fault geometry. We used the Sentinel 2 optical imagery pixel offsets, as noted in Section 2.1 to define the surface expression of the fault (blue line in Figure 1A,B) and the first 2 weeks of aftershocks from the Thai regional network (Pornsopin, 2023, Figure 1B) to define the approximate extent of faulting, we note that the aftershock locations are biased east of the surface trace, this is most likely an artifact, one-sided networks with large azimuthal gaps can have systematic biases like these (e.g. Bondar et al., 2004). We assumed a seismogenic depth (the maximum extent of slip) of 20 km in line with other reports (e.g. Tun & Watkinson, 2017; Tin et al. (2022) that determined locking depths from seismicity and inversions of regional GNSS measurements of the interseismic velocity field. Finally, we discretized the fault into triangular subfaults using a 3D mesher. To account for the depth dependent resolution of slip inversions (e.g. Xu et al., 2016) we used progressively coarsening subfaults with depth. From 0 to 2.5 km subfaults have ~4 km vertices, from 2.5 to 10 they have ~7 km vertices and from 10 to 20 km they have ~10 km vertices. For simplicity, we first assumed a vertical dip; this geometry can be seen in Figure 5A. Additionally, we built a second "variable dip" geometry based on the geodetic inversion results of Tin et al. (2022). That work concluded that the interseismic velocity field was best explained by a fault that had vertical dip south of ~20°N, a 78° westward dip between ~20°N and ~21.5°N and then a 71° eastward dip northward of 21.5°N. We produced kinematic models on this “corkscrew” geometry as well to test whether the data preferred one or the other. This geometry can be seen in Figure 5B, and each model has ~850 sub faults.

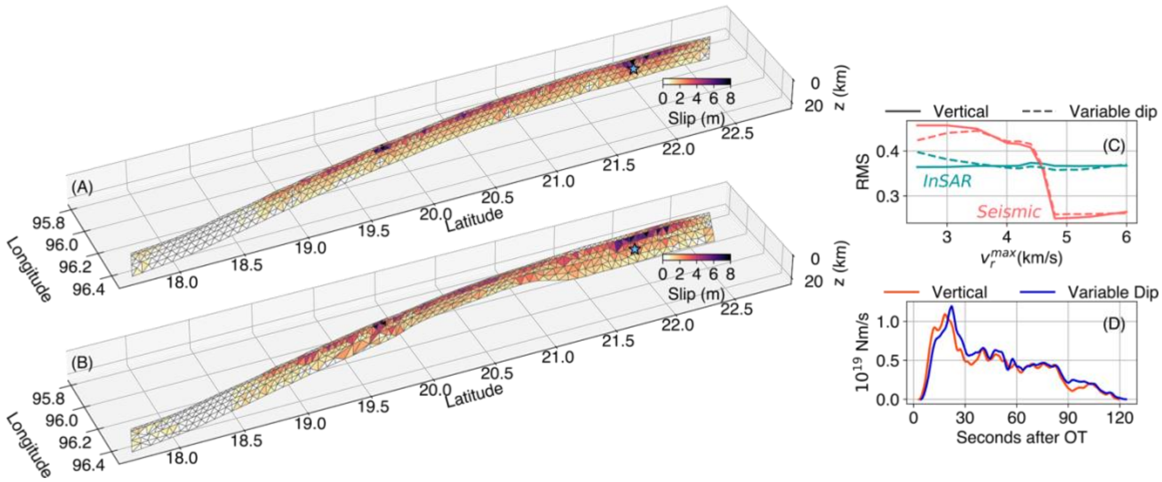

Figure 5. *(A) Perspective view of the best-fit rupture model assuming a purely vertical geometry. Blue star is the assumed hypocenter. (B) same as (A) but with a variable-dip geometry. (C) RMS misfits as a function of maximum allowed rupture speed for both InSAR and seismic data for each of the two geometries. Lowest misfits occur at ~4.8 km/s. (D) Source time functions for the preferred models showing a rupture duration of 90-120 s.*

We carry out kinematic slip inversion using the multi-time-window method described by Melgar & Bock, 2015, which allows for flexible rupture timing across the fault by assigning multiple overlapping source time functions to each subfault; 8 overlapping triangles with 4 s rise time re allowed for each. This 4 s rise time is consistent with what is expected from an M7.8 earthquake from analysis of global earthquakes (Melgar et al., 2017). Observed ground displacement time series from integrated strong motion, and the pixel offsets from InSAR are jointly inverted to estimate the spatial and temporal distribution of fault slip. To ensure balanced contributions from each data type, we normalized the residuals by the L2 norm of each dataset, effectively weighting them equally in the objective function (e.g. Melgar et al., 2020). Rupture initiation was assumed to occur at the hypocenter reported by the U.S. Geological Survey at 2025-03-28 06:20:52 (UTC) at 22.001°N, 95.925°E, and 10.0 km depth. Several maximum allowable rupture speeds were tested, ranging from 3.0 to 6.0 km/s, to explore sensitivity of the inversion to this constraint. The inversion is stabilized using Tikhonov regularization and the final model was selected based on the L-curve criterion

2.4 Paleoseismology

We document displacement and frequency of surface ruptures from historic and paleoseismic earthquakes on the Sagaing Fault at a site (Figure 1B,6A) near the 2025 M7.8 epicenter 4 km NW of Mandalay. In the context of a field-training school funded by the Earth Observatory of Singapore and including students from Myanmar, five other SE Asian countries, China, and USA from 2016 to 2018, we chose a portion of the Sagaing Fault where the active trace diverges from the range front (Figure 7) and trends more westerly (northern two-thirds of Figure 6B), causing compression and uplifting low hills that block stream flow and thus rapidly accumulates young sediment that includes abundant ^{14}C samples and Buddhist-era artifacts we use for age control (Figure 8E). Using drone imagery (Figure 7) and ground-based LiDAR we mapped geomorphic offsets and excavated 18 trenches to reveal deformation associated with past earthquakes. Here we focus on a group of trenches in the southern half of the area (central portions of Figures 6B,7) where the age and displacement associated with the five surface ruptures before 2025 can be estimated.

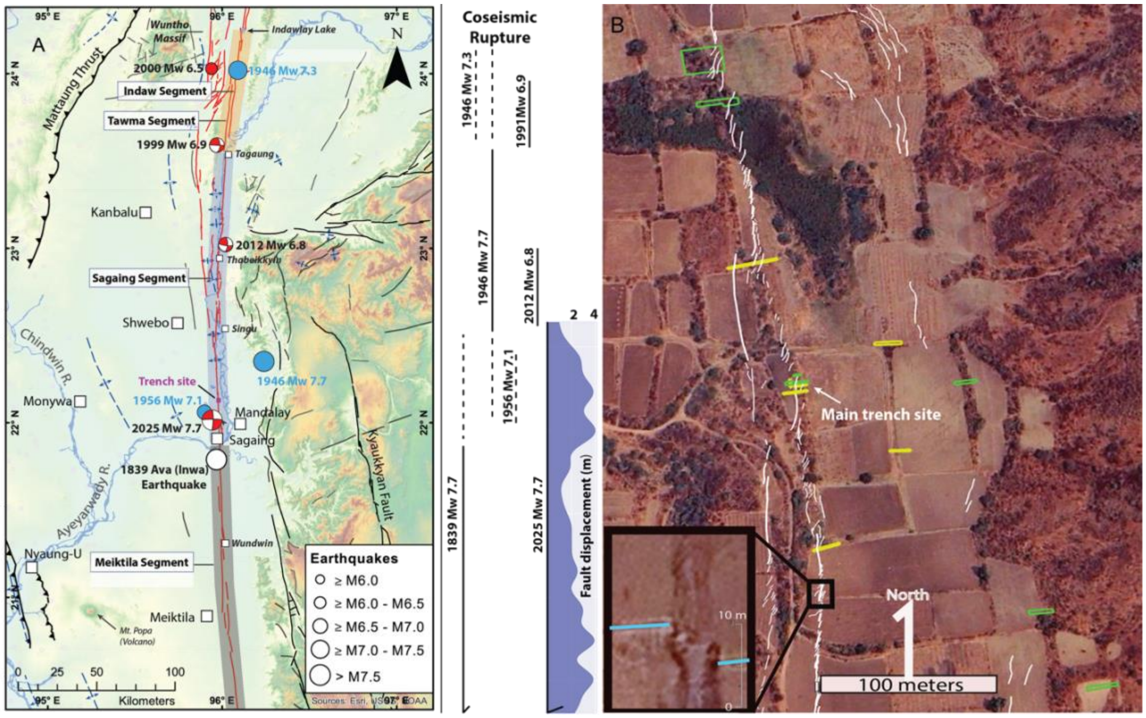

Figure 6. *(A) Historic earthquakes and paleoseismic site plotted on a geologic map of the Sagaing Fault (updated from Wang et al. 2014). Regional location shown in Figure1B. Colored rectangles along the fault are the Indaw, Tawma, Sagaing, and Meiktila fault segments (Wang et al., 2014). Blue circles are inferred event hypocenters for historical earthquakes from Hurukawa & Maung (2011) and Wang et al. (2014) and rupture extents of historic surface ruptures (dashed where uncertain) are on right side with along-strike displacement shown for 2025. Shown as well is the depth-averaged displacement from our preferred slip model. (B) Post 2025 earthquake Google Earth image of the southern half of the paleoseismic study site. White lines are visible surface ruptures, green are 2016 trenches, yellow 2018 trenches and box in SW corner locates one of many 4-5m offsets (blue lines are an offset trail) in 2025 along this portion of the fault. Trenches east of the main trace were excavated to confirm that geomorphic lineaments were not recently active, although scattered cracks from the 2025 rupture indicate that the range front is not completely inactive. Westernmost white lines indicate cracks along the back edge of the uplifted hills that was only exposed in one trench. Figures 7,8 are located in the center where 2016 and 2018 trenches are clustered and have the best evidence for the timing and displacement of recent earthquakes.*

We attempted to reconstruct the coseismic displacements at this site and can now compare how the 2025 offsets relate to past ruptures. To estimate the vertical component of slip associated with prehistoric surface-rupturing earthquakes, we applied a geomorphic approach (Figure 9) based on the formation of colluvial wedges at fault scarps. Following a surface-rupturing event, the exposed scarp undergoes gravitational collapse and subsequent erosion, depositing a wedge-shaped body of debris on the downthrown block. Experimental and field observations demonstrate that the maximum thickness of such a wedge is typically about half the height of the original fault scarp (Wallace, 1977; Nash, 1980; Avouac and Peltzer, 1993).

We use this geometric relationship to infer the height of paleo-scarps—and by extension, the vertical displacement—by measuring the preserved maximum thickness of buried colluvial wedges in the trench exposures. This method has been applied in previous studies, notably by Klinger et al. (2003), who argued that colluvial wedges of ~0.8 m thickness corresponded to ~1.6 m of vertical slip during repeated events on a normal-faulting step-over along the North Anatolian Fault. Their analysis showed that wedge thicknesses can serve as reliable proxies for scarp height, particularly in settings where vertical displacement dominates and preservation conditions are favorable.

Figure 7. *Drone image looking north, taken during 2018 field work showing several trenches and how the main fault diverges from the range front to uplift a row of hills that block drainage from the mountains to the east (right) and causes accumulation of young sediment against the fault zone. Drone flyover videos are available as Supplementary Files S1 and S2 (see Data and Code Availability)*

In our analysis, we adopt the same 2:1 ratio (scarp height to wedge thickness) as a first-order approximation of vertical offset for each scarp-forming event identified in the stratigraphy, which collectively measure 1.6 m in thickness (the youngest is too modified due to cultural activity associated with local agriculture), yielding an average of 40 cm per event (Figure 8A,B)—so we infer that individual events have vertical displacement of ~80 cm. Given the orientation of this portion of the fault (measured across the eight walls in the map in Figure 8A, similar to the orientation at the trench site in Figure 6A) relative to the orientation of pure strike-slip portions nearby, we would expect the vertical to be about 20% of the horizontal, so the average horizontal displacement would be about 4 m. This is consistent with the 2025 rupture and fluvial sediments seen in the lowest wedge (blue in Figure 8C) that likely came from a small stream now followed by the road ~20 m to the north.

We are a working on a more complete 3D reconstruction of the wedges and fault traces using all eight exposures of the fault zone shown in the map in Figure 6B,8A which will allow us to make a better determination of the thicknesses and possibly offsets of individual wedges and to put all of our ^{14}C samples into a single stratigraphic column to make the best age model possible.

3. Results and discussion

3.1 The Earthquake Source

The slip inversion results in Figure 5A,B show significant slip from the hypocenter north to ~22.2N and south to at least 18.5N for a full rupture length of ~450 km. Slip is highest between the surface an 10 km depth and tapers from there to 20 km. Depth averaged slip is ~3-5m across the rupture (e.g. Figure 6A) with localized small patches of higher amplitude slip as high as 7-8 m. The total magnitude for the event from inversion depending on whether the vertical or variable dip geometry is preferred is M 7.75 - 7.79. This means the long rupture length is somewhat anomalous compared to the mean expected length of 186 km for this magnitude from the probabilistic scaling laws of Blaser et al. (2010), placing it at the 98th percentile of expected rupture lengths.

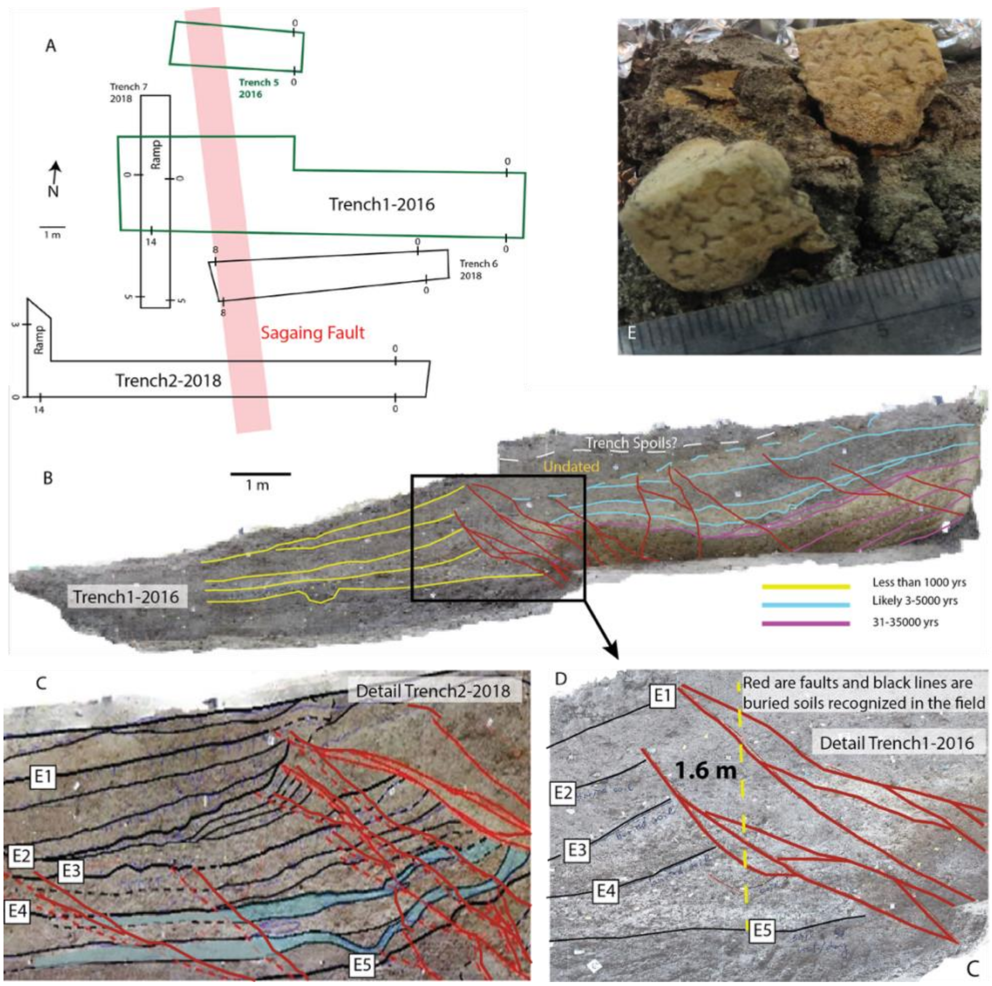

Figure 8. *(A) Simplified map of trenches excavated between 2016-2018 (location is in Figure 6) (B) Example of a trench (Trench1-2016) across the main trace. (C) detail of the main fault zone from Trench2-2018. We recognize 5 pre2025 ruptures (E1-E5) and collected abundant charcoal and cow+ bones for ^{14}C samples and pottery to date the ruptures. Upward termination of individual fault surfaces and soil-capped colluvial wedges generated by individual earthquakes allow us to characterize and date events from the past ~1000 years. Light blue layers between E4 & E5 are from a laterally offset ~20 m from a small stream across the fault (Figure 6B), suggesting average lateral slip of 4-5 m per event. (D) Same as (C) for Trench1-2016. The aggregate width of colluvial wedges for E2-E5 was measured 1.6 m corresponding ~40 cm per wedge per event (E) Example of pottery found in several of our trenches; this pattern is first seen in this area in the 11th century (Guy, 1989).*

In terms of its kinematics, even without an analysis of the inversion, we cand conclude the rupture is most likely super-shear. Station NPW on the surface trace of the fault (Figures 1A,2) shows a clear slip pulse with large fault parallel ground motions. The dashed lines on that figure show how quickly a rupture front would have to propagate from the catalog hypocenter along the Sagaing Fault to reach NPW. This simple analysis suggests strongly that the pulse needs to be traveling at just under 5 km/s. This is in fact confirmed by the slip inversion results shown in Figure 5C which shows that the best RMS misfit to the regional strong motion data is for a maximum rupture speed of 4.8 km/s. Indeed, at this rupture speed, the fits to the strong motion waveforms (Figure 10), in particular station NPW, are quite good with the exception of the north and vertical components at station YGN at the southern terminus of the rupture (Figure 1B). As noted by Thiam et al. (2017) YGN is on the soft sediments from the Ayeyarwady and Sitang River deltas and likely has significant site amplification effects we are not capturing with our simple 1D velocity structure. Likewise, both ascending and descending SAR pixel offset scenes show good fits (Figure 11) with no significant biases in the residual patterns. These results do not allow us to say conclusively whether the vertical or variable dip geometry are preferred as they both fit the data to similar levels. Finally, we note that given the significant fault length, and despite the fast rupture propagation the source duration is long (Figure 5D) lasting as much as 120 s. However, the moment released between 90 and 120 s is from slip at the southern terminus of the rupture and most likely spurious and an attempt by the inversion process to fit later arrivals at YGN, the southernmost site. The more likely source duration is closer to ~90 s.

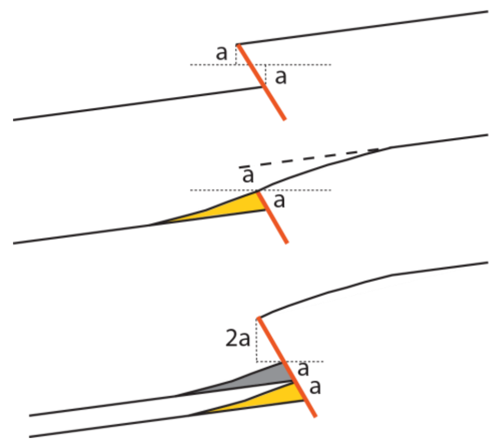

Figure 9. *Cartoon (modified from Klinger et al 2003) shows the relationship between the vertical component of slip and scarp wedge thickness, suggesting ~1 m of vertical slip per event, similar to the 2025 scarp at the site (Figure 8)*

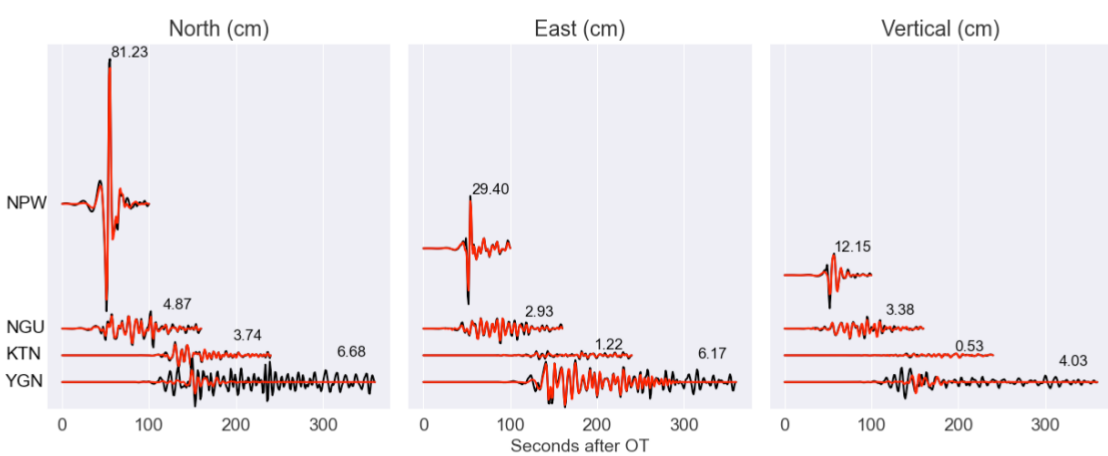

Figure 10. *Inversion waveform fits, black is the data and red the synthetics. Peak values for each station are indicated next to each waveform. Note that stations NGU, KTN, and YGN are presented with a factor of 2 larger amplitude for clarity.*

3.2 A history of overlapping ruptures at the northern terminus of the 2025 event

Preliminary results from our mapping, trenches, and age control provide evidence for five surface ruptures that occurred at the site in the ~1000 years before 2025. This includes post-bomb ^{14}C dates consistent with either or both of the 1946/1956 sequences, stratigraphically consistent ^{14}C represents

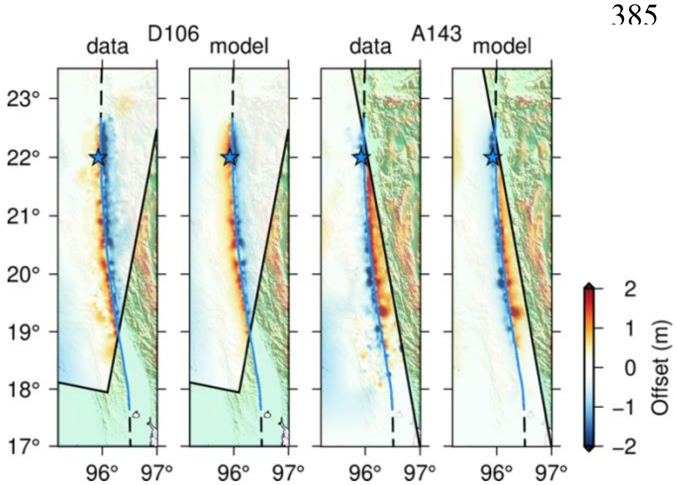

Figure 11. *Comparison between observed azimuth offsets after median filtering (labeled "data" and described in Section 2.2) and the modeled offsets predicted by the best fitting slip inversion. The blue star is the event hypocenter and the blue line the inferred fault geometry. The black dashed line is the inferred surface trace of the Sagaing fault not used in the inversion*

the 1839 event. Buddhist-era pottery limits the past five events to less than ~1000 years (Figure 8). Although displacement per event, based largely on colluvial wedge thickness and the ratio of vertical to horizontal slip (Figure 8), appears to vary by at least a factor of 2, the average displacement of the previous five events (or sequence if close in time like 1946/56) is 4-5 meters, similar to the 2025 fault displacement at the site (Figure 6A).

This last point is notable. For an average slip rate of 20 mm/yr, the 4-5 m of coseismic slip on this segment of the fault inferred from paleoseismology and observed in 2025 requires 200-250 yrs to accumulate. That time is far shorter than the inter-event time we report here and suggests that ruptures on this part of the Sagaing fault cluster closely in time. Whether large ruptures on major continental transforms cluster, are random, or quasi-periodic has been the subject of debate (e.g. Scharer et al., 2010). We also note that in this trench we dated only the purple layers in the upthrown (right) side of the fault; however, 3000-5000 yr old ^{14}C (charcoal) samples mixed with pottery and many ^{14}C samples less than 1000 years in the colluvial wedges suggest that the source of the wedges was 3000-5000 years old. Ongoing work on a 3D reconstruction and age model including all eight trench walls will help elucidate the detailed timing and displacement history here.

Furthermore, it is worth speculating on whether the short segment of the fault surrounding Mandalay is routinely the initiation point of large ruptures. Based on the paleoseismic record, with the new data from the 2025 rupture to supplement it, it appears that this portion of the fault often nucleates large ruptures that propagate either north or south and thus are centered more north (1946) and south (1839 & 2025) of the site.

Finally, we point out that the historic events and the 2025 earthquake suggest that the boundary between the Sagaing and Meiktila segments of the fault (Figure 6A) is rather diffuse. The inferred history shows that events that rupture both north and south overlap near the trench site. This suggests that the boundary is not a strict barrier. Whether the other segments behave likewise is at present unknown and is further evidence of the need for more concerted paleoseismic work along the entirety of the fault.

3.3 Implications for hazards

The super-shear kinematics of this event add to the recent observations of similar behavior in other large transform faults such as the 2018 Palu, 2021 Maduo, 2023 Turkïye earthquakes (Bao et al., 2019; Zhang et al, 2022; Melgar et al., 2023). How super-shear kinematics affect ground motion can be complex—modeling has shown that super-shear source processes can reduce ground motion immediately adjacent to the fault but increase it elsewhere (Dunham & Bhat, 2008; Andrews, 2010). These observations and models argue that super-shear ruptures are more common than previously considered and potentially not captured correctly in ground motion models. While it is difficult to interpret them without ambiguity, the Did You Feel It Reports from the USGS are biased high (USGS, 2025), meaning they systematically indicate stronger than expected shaking for this event when compared to ground motion models. Is this due to the super-shear kinematics? And, can we expect all large events on this fault system to always exhibit this behavior? Accounting for this extra "source effect" and the uncertainty it adds to hazard calculations seems pressing.

In terms of future hazards calculations for the Sagaing it is difficult to say what this event foretells for the region. Significant amounts of slip have been released and, significantly, most of the 2025 rupture last slipped in 1839. That inter-event interval allows for 3.8 m of slip deficit, most, if not all, of which would have been released in 2025. However, as evidenced by the event clusters in the trenches near Mandalay, it is plausible that slip deficit from earlier on in the seismic cycle remains available and unused. Without further paleoseismology elsewhere on the fault it is not feasible to say with any confidence whether the 2025 rupture significantly reduces hazard.

Conceptually, however, from simple Coulomb stress triggering arguments, and as seen on other transform systems, most famously in the Northern Anatolian fault (e.g. Stein et al., 1997), it would seem that the southern segments of the fault adjacent to the terminus of the 2025 rupture are of most concern—they have the fewest historic events and likely a large accumulated slip deficit. The last rupture here was an ~M7.2 earthquake in 1930 (Tsutumi & Sato, 2009) and cumulative recurrence intervals for this segment have been inferred to be as short as 90-115 years (Wang et al., 2011). Whatever the case, the region is populous (Figure 1A)—this enormous exposure when combined with precarious construction practices continues to place the Sagaing fault as potentially one of the most deadly continental transform faults in the world.

4. Conclusions

The 2025 Mw 7.8 earthquake along the central Sagaing Fault represents one of the most significant and destructive seismic events in Southeast Asia in recent history. Our joint kinematic inversion of regional strong motion and SAR pixel offset data reveals a ~450 km rupture with 3–5 m of average slip and supershear rupture propagation at ~4.8 km/s. This event adds to a growing list of well-documented supershear ruptures on major continental strike-slip faults, with important implications for ground motion prediction and seismic hazard assessments. At a key paleoseismic site near the epicenter, we document evidence for five past surface-rupturing earthquakes over the past millennium with comparable displacement, indicating repeated rupture of the same fault segment and suggesting that this section of the Sagaing Fault is both a persistent nucleation zone and a locus of overlapping ruptures. These findings challenge models of strict fault segmentation and point to the need for reevaluation of seismic hazard across the broader fault system. The densely populated corridor along the Sagaing Fault remains acutely vulnerable, and our results underscore the urgent need for improved hazard mapping, infrastructure resilience, and expanded paleoseismic investigations across the fault's length.

Acknowledgements

We thank Kerry Sieh for his generous support and advocacy in funding fieldwork through the Earth Observatory of Singapore at Nanyang Technological University, and for discussions of paleoseismology of the Sagaing Fault. This work was partially funded by NASA grant 23-ESI23-0012 to the University of Oregon and JPL teams. We acknowledge support as well from National Science and Technology Council grants 112-2116-M-002-007 and 113-2116-M-002 –028 to YW.

Data and code availability

All data needed to run the inversion as well as inversion results are available in our Zenodo supplement at https://doi.org/10.5281/zenodo.15529796. Strong motion data for stations KTN, NGU and YGN is from Network MM operated by the Myanmar Department of Meteorology and Hydrology

(2016). Data for station NPW is from network GE from GEOFON (1993). Kinematic slip inversion code MudPy is open source archived at Melgar et al. (2021) and available at https://github.com/UO-Geophysics/MudPy. This work utilized modified Copernicus data from Sentinel-1A/B and Sentinel-2A, -2B, and -2C satellites acquired and provided by the European Space Agency (ESA; 2025). Original Sentinel-1 and Sentinel-2 data are available from the Copernicus Data Space Ecosystem (https://dataspace.copernicus.eu/), and Sentinel-1 data are also available from the Alaska Satellite Facility data archive (https://asf.alaska.edu/asfsardaac/). Processed optical and SAR pixel offset data are available on our Zenodo supplement and through the aria-share repository at https://aria-share.jpl.nasa.gov/20250328_Myanmar_EQ/ .

Competing interests

The authors declare that they have no competing interests.

References

Andrews, D. J. (2010). Ground motion hazard from supershear rupture. Tectonophysics, 493(3-4), 216-221.

Avouac, J.-P., and G. Peltzer (1993). Active tectonics in southern Zinjiang, China: analysis of terrace riser and normal fault scarp degradation along the Hotan–Qira fault system, J. Geophys. Res. 98, no. B12, 773–807.

Avouac, J.-P., & Leprince, S. (2015). Geodetic imaging using optical systems. In G. Schubert (Ed.), Treatise on Geophysics (pp. 387–424). Oxford: Elsevier.

Bao, H., Ampuero, J. P., Meng, L., Fielding, E. J., Liang, C., Milliner, C. W., ... & Huang, H. (2019). Early and persistent supershear rupture of the 2018 magnitude 7.5 Palu earthquake. *Nature Geoscience*, *12*(3), 200-205.

Bato, M. G., Lundgren, P., Pinel, V., Solidum Jr, R., Daag, A., & Cahulogan, M. (2021). The 2020 eruption and large lateral dike emplacement at Taal volcano, Philippines: Insights from satellite radar data. *Geophysical Research Letters*, *48*(7), e2021GL092803.

Blaser, L., Krüger, F., Ohrnberger, M., & Scherbaum, F. (2010). Scaling relations of earthquake source parameter estimates with special focus on subduction environment. *Bulletin of the Seismological Society of America*, *100*(6), 2914-2926.

Bondár, I., Myers, S. C., Engdahl, E. R., & Bergman, E. A. (2004). Epicentre accuracy based on seismic network criteria. *Geophysical Journal International*, *156*(3), 483-496.

Casu, F., Manconi, A., Pepe, A., & Lanari, R. (2011). Deformation time-series generation in areas characterized by large displacement dynamics: The SAR amplitude pixel-offset SBAS technique. *IEEE Transactions on Geoscience and Remote Sensing*, *49*(7), 2752-2763.

Curray, J. R. (2005). Tectonics and history of the Andaman Sea region. *Journal of Asian Earth Sciences*, *25*(1), 187-232.

Deng, Q., Zhang, P. Colluvial wedges associated with pre-historical reverse faulting paleoearthquakes. *Chin.Sci.Bull.* **45**, 1598–1604 (2000).

Department of Meteorology and Hydrology - National Earthquake Data Center. (2016). *Myanmar National Seismic Network* [Data set]. International Federation of Digital Seismograph Networks. https://doi.org/10.7914/SN/MM

Drusch, M., Del Bello, U., Carlier, S., Colin, O., Fernandez, V., Gascon, F., Hoersch, B., Isola, C., Laberinti, P., Martimort, P. and Meygret, A., (2012). Sentinel-2: ESA's optical high-resolution mission for GMES operational services. Remote sensing of Environment, 120, pp.25-36

Dunham, E. M., & Bhat, H. S. (2008). Attenuation of radiated ground motion and stresses from three-dimensional supershear ruptures. *Journal of Geophysical Research: Solid Earth*, *113*(B8).

Dziewonski, A. M., & Anderson, D. L. (1981). Preliminary reference Earth model. *Physics of the earth and planetary interiors*, *25*(4), 297-356.

Earle, P. S., Wald, D. J., Jaiswal, K. S., Allen, T. I., Hearne, M. G., Marano, K. D., ... & Fee, J. M. (2009). Prompt Assessment of Global Earthquakes for Response (PAGER): A system for rapidly determining the impact of earthquakes worldwide. *US Geological Survey Open-File Report*, *1131*(2009), 15.

Ekström, G., Nettles, M., & Dziewoński, A. M. (2012). The global CMT project 2004–2010: Centroid-moment tensors for 13,017 earthquakes. *Physics of the Earth and Planetary Interiors*, *200*, 1-9.

Gahalaut, V. K., and K. Gahalaut (2007), Burma plate motion, *J. Geophys. Res.*, 112, B10402, doi:10.1029/2007JB004928.

Gardner, A.S., Moholdt, G., Scambos, T., Fahnstock, M., Ligtenberg, S., Broeke, M.V.D. and Nilsson, J., 2018. Increased West Antarctic and unchanged East Antarctic ice discharge over the last 7 years. The Cryosphere, 12(2), pp.521-547.

GEOFON Data Centre. (1993). *GEOFON Seismic Network* [Data set]. GFZ Data Services.

Guy, J. (1990). Ceramic Traditions of SE Asia, Oxford University Press, 80pp.

Hlaing, R., Gunawan, E. , Widiyantoro, S., Meilano, I., Saepuloh, A. (2019). Assessment of the maximum magnitude of strike-slip faults in Myanmar. *Geotechnical and Geological Engineering* **37**, 5113-5122,, doi:10.1007/s10706-019-00965-3.

Hurukawa, N., & Maung, P. (2011). Two seismic gaps on the Sagaing Fault, Myanmar, derived from relocation of historical earthquakes since 1918. *Geophysical Research Letters*, *38*(1).

Kennett, B. L. N., & Engdahl, E. R. (1991). Traveltimes for global earthquake location and phase identification. *Geophysical Journal International*, *105*(2), 429-465.

Klinger, Y., K. Sieh, E. Altunel, A. Akoglu, A. Barka, T. Dawson, T. Gonzalez, A. Meltzner, T. Rockwell (2003). Paleoseismic Evidence of Characteristic Slip on the Western Segment of the North Anatolian Fault, Turkey. *Bull. Seism. Soc. Am.*; 93 (6): 2317–2332. doi: 10.1785/0120010270.

Lai, S.-T., Oo, K. M., Htwe, Y. M. M., Yi, T., Than, H. H., Than, O., Min, Z., Oo, T. M., Maung, P. M., Bindi, D., Cotton, F., Evans, P. L., Heinloo, A., Hillmann, L., Saul, J., Sens-Schoenfelder, C., Strollo, A., Tilmann, F., Weatherill, G., Yen, M.-H., Zaccarelli, R., Zieke, T., and Milkereit, C.: Capacity Building Enables Unique Near-Fault Observations of the destructive 2025 M_w 7.7 Myanmar Earthquake, Earth Syst. Sci. Data Discuss. [preprint], https://doi.org/10.5194/essd-2025-216, in review, 2025.

Lebakula, V., Epting, J., Moehl, J., Stipek, C., Adams, D., Reith, A., Kaufman, J., Gonzales, J., Reynolds, B., Basford, S., Martin, A., Buck, W., Faxon, A., Cunningham, A., Roy, A., Barbose, Z., Massaro, J., Walters, S., Woody, C., ... Urban, M. (2024). *LandScan Silver Edition* [Data set]. Oak Ridge National Laboratory. https://doi.org/10.48690/1531770

Lei, Y., Gardner, A. and Agram, P., 2021. Autonomous Repeat Image Feature Tracking (autoRIFT) and Its Application for Tracking Ice Displacement. Remote Sensing, 13(4), p.749.=

Le Dain, A. Y., Tapponnier, P., & Molnar, P. (1984). Active faulting and tectonics of Burma and surrounding regions. *Journal of Geophysical Research: Solid Earth*, *89*(B1), 453-472.

Lindsey, E.O., et al. (2023), Active subduction and strain partitioning in western Myanmar revealed by a dense survey GNSS network. *Earth Planet, Sci. Lett.* **622**, 118384, doi:10.1016/j.epsl.2023.118384.

Mallick, R., Lindsey, E. O., Feng, L., Hubbard, J., Banerjee, P., & Hill, E. M. (2019). Active convergence of the India‐Burma‐Sunda plates revealed by a new continuous GPS network. *Journal of Geophysical Research: Solid Earth*, *124*(3), 3155-3171.

Maung, H. (1987). Transcurrent movements in the Burma–Andaman Sea region. *Geology*, *15*(10), 911-912.

Maurin, T., Masson, F., Rangin, C., Min, U. T., & Collard, P. (2010). First global positioning system results in northern Myanmar: Constant and localized slip rate along the Sagaing fault. *Geology*, *38*(7), 591-594.

McCalpin, J.P. (2009) Paleoseismology. 2nd Edition, Academic Press, Amsterdam-London, 615 p.

Melgar, D., & Bock, Y. (2015). Kinematic earthquake source inversion and tsunami runup prediction with regional geophysical data. *Journal of Geophysical Research: Solid Earth*, *120*(5), 3324-3349.

Melgar, D., & Hayes, G. P. (2017). Systematic observations of the slip pulse properties of large earthquake ruptures. *Geophysical Research Letters*, *44*(19), 9691-9698.

Melgar, D., Ganas, A., Taymaz, T., Valkaniotis, S., Crowell, B. W., Kapetanidis, V., ... & Öcalan, T. (2020). Rupture kinematics of 2020 January 24 M w 6.7 Doğanyol-Sivrice, Turkey earthquake on the East Anatolian Fault Zone imaged by space geodesy. *Geophysical Journal International*, *223*(2), 862-874.

Melgar, D., Lin, J.-T, Kong, Q., Ruhl, Q. & Marfito, B. (2021). dmelgarm/MudPy: v1.3 (v1.3). Zenodo. https://doi.org/10.5281/zenodo.5397091

Melgar, D., Taymaz, T., Ganas, A., Crowell, B. W., Öcalan, T., Kahraman, M., ... & Altuntaş, C. (2023). Sub-and super-shear ruptures during the 2023 Mw 7.8 and Mw 7.6 earthquake doublet in SE Türkiye.

Mon, C. T., Gong, X., Wen, Y., Jiang, M., Chen, Q.-F., Zhang, M., et al. (2020). Insight into major active faults in Central Myanmar and the related geodynamic sources. *Geophysical Research Letters*, 47, e2019GL086236. https://doi.org/10.1029/2019GL086236

Morley, C.K. and Arboit, F., 2019. Dating the onset of motion on the Sagaing fault: Evidence from detrital zircon and titanite U-Pb geochronology from the North Minwun Basin, Myanmar. Geology, 47(6): 581-585.

National Research Council (2007). *Tools and methods for estimating populations at risk from natural disasters and complex humanitarian crises*. National Academies Press, 1st ed., 264 pp.

Nash, D. B. (1980). Morphologic dating of degraded normal fault scarps, J. Geol. 88, 353–360.

Panda, D., Kundu, B., Gahalaut, V. K., & Rangin, C. (2018). Crustal deformation, spatial distribution of earthquakes and along strike segmentation of the Sagaing Fault, Myanmar. *Journal of Asian Earth Sciences*, *166*, 89-94.

Pasyanos, M. E., Masters, T. G., Laske, G., & Ma, Z. (2014). LITHO1. 0: An updated crust and lithospheric model of the Earth. *Journal of Geophysical Research: Solid Earth*, *119*(3), 2153-2173.

Pathier, E., Fielding, E. J., Wright, T. J., Walker, R., Parsons, B. E., & Hensley, S. (2006). Displacement field and slip distribution of the 2005 Kashmir earthquake from SAR imagery. *Geophysical research letters*, *33*(20).

Pornsopin, P., Pananont, P., Furlong, K. P., & Sandvol, E. (2023). Sensor orientation of the TMD seismic network (Thailand) from P-wave particle motions. *Geoscience Letters*, *10*(1), 24.

Rosen, P. A., Gurrola, E., Sacco, G. F., & Zebker, H. (2012). The InSAR scientific computing environment. In *EUSAR 2012; 9th European conference on synthetic aperture radar* (pp. 730-733). VDE.

Scharer, K. M., Biasi, G. P., Weldon, R. J., & Fumal, T. E. (2010). Quasi-periodic recurrence of large earthquakes on the southern San Andreas fault. *Geology*, *38*(6), 555-558.

Shi, X., Wang, Y., Sieh, K., Weldon, R., Feng, L., Chan, C.-H., & Liu-Zeng, J. (2018). Fault slip and GPS velocities across the Shan Plateau define a curved southwestward crustal motion around the eastern Himalayan syntaxis. *Journal of Geophysical Research: Solid Earth*, 123, 2502–2518. https://doi.org/10.1002/2017JB015206

Socquet, A., Vigny, C., Chamot-Rooke, N., Simons, W., Rangin, C., & Ambrosius, B. (2006). India and Sunda plates motion and deformation along their boundary in Myanmar determined by GPS. *Journal of Geophysical Research: Solid Earth*, *111*(B5).

Steckler, M., Mondal, D., Akhter, S. *et al.* Locked and loading megathrust linked to active subduction beneath the Indo-Burman Ranges. *Nature Geosci* **9**, 615–618 (2016). https://doi.org/10.1038/ngeo2760

Strozzi, T., Luckman, A., Murray, T., Wegmuller, U., & Werner, C. L. (2002). Glacier motion estimation using SAR offset-tracking procedures. *IEEE Transactions on Geoscience and Remote Sensing*, *40*(11), 2384-2391.

Thein, M., Myint, T., Tun, S.T. and Swe, T.L., (2009). Earthquake and tsunami hazard in Myanmar. Journal of Earthquake and Tsunami, 3(02): 43-57.

Thiam, H. N., Htwe, Y. M. M., Kyaw, T. L., Tun, P. P., Min, Z., Htwe, S. H., ... & Hough, S. E. (2017). A report on upgraded seismic monitoring stations in Myanmar: Station performance and site response. *Seismological Research Letters*, *88*(3), 926-934.

Tin, T. Z. H., Nishimura, T., Hashimoto, M., Lindsey, E. O., Aung, L. T., Min, S. M., & Thant, M. (2022). Present-day crustal deformation and slip rate along the southern Sagaing fault in Myanmar by GNSS observation. *Journal of Asian Earth Sciences*, *228*, 105125.

Tsutsumi, H., & Sato, T. (2009). Tectonic geomorphology of the southernmost Sagaing fault and surface rupture associated with the May 1930 Pegu (Bago) earthquake, Myanmar. *Bulletin of the Seismological Society of America*, *99*(4), 2155-2168.

Tun, S.T & Watkinson, I.M. (2017). The Sagaing Fault, Myanmar, in: Myanmar: Geology, Resources and Tectonics, A. J. Barber, Khin Zaw, M. J. Crow eds. DOI:10.1144/M48.19

U.S. Geological Survey (USGS) Earthquake Hazards Program (2017). Advanced National Seismic System (ANSS) comprehensive cata-log of earthquake events and products, U.S. Geol. Surv. Data Release, doi: 10.5066/F7MS3QZH

U.S. Geological Survey (2025) M 7.7 - 2025 Mandalay, Burma (Myanmar) Earthquake, https://earthquake.usgs.gov/earthquakes/eventpage/us7000pn9s/pager

Wald, D., Jaiswal, K., Marano, K., Earle, P., & Allen, T. (2010). Advancements in casualty modelling facilitated by the USGS Prompt Assessment of Global Earthquakes for Response (PAGER) System. In *Human casualties in earthquakes: progress in modelling and mitigation* (pp. 221-230). Dordrecht: Springer Netherlands.

Wallace, R. E. (1977). Profiles and ages of young fault scarps, north-central Nevada, Geol. Soc. Am. Bull. 88, 1267–1281.

Wang, Y., Sieh, K., Aung, T., Min, S., Khaing, S. N., & Tun, S. T. (2011). Earthquakes and slip rate of the southern Sagaing fault: insights from an offset ancient fort wall, lower Burma (Myanmar). *Geophysical Journal International*, *185*(1), 49-64.

Wang, Y., Sieh, K., Tun, S. T., Lai, K. Y., & Myint, T. (2014). Active tectonics and earthquake potential of the Myanmar region. *Journal of Geophysical Research: Solid Earth*, *119*(4), 3767-3822.

Weldon, R., K. Scharer, T. Fumal, G. Biasi (2004). Wrightwood and the earthquake cycle: What a long recurrence record tells us about how faults work. *GSA Today* **14** (9), 4-10,

Xiong, X., Shan, B., Zhou, Y. M., Wei, S. J., Li, Y. D., Wang, R. J., & Zheng, Y. (2017). Coulomb stress transfer and accumulation on the Sagaing Fault, Myanmar, over the past 110 years and its implications for seismic hazard. *Geophysical Research Letters*, *44*(10), 4781-4789.

Xu, X., Tong, X., Sandwell, D. T., Milliner, C. W., Dolan, J. F., Hollingsworth, J., ... & Ayoub, F. (2016). Refining the shallow slip deficit. *Geophysical Journal International*, *204*(3), 1867-1886.

Yang, S., Xiao, Z., Wei, S., He, Y., Mon, C. T., Hou, G., et al. (2024). New insights into active faults revealed by a deep-learning-based earthquake catalog in central Myanmar. *Geophysical Research Letters*, 51, e2023GL105159. https://doi.org/10.1029/2023GL105159

Zhang, X., Feng, W., Du, H., Samsonov, S., & Yi, L. (2022). Supershear rupture during the 2021 MW 7.4 Maduo, China, earthquake. *Geophysical Research Letters*, *49*(6), e2022GL097984.

Zheng, G., et. al. (2017). Crustal deformation in the India-Eurasia collision zone from 25 years of GPS measurements. *J. Geophys. Res.* **122** (11), 9290-9312, doi:10.1002/2017jb014465.